Veering and Nonlinear Interactions of a Clamped Beam in Bending and Torsion

David A. Ehrhardt, Thomas L. Hill, Simon A. Neild, and Jonathan E. Cooper
Department of Mechanical Engineering, University of Bristol, Bristol, UK

Abstract
Understanding the linear and nonlinear dynamic behaviour of beams is critical for the design of many engineering structures such as spacecraft antennae, aircraft wings, and turbine blades. When the eigenvalues of such structures are closely-spaced, nonlinearity may lead to interactions between the underlying linear normal modes (LNMs). This work considers a clamped-clamped beam which exhibits nonlinear behaviour due to axial tension from large amplitudes of deformation. An additional cross-beam, mounted transversely and with a movable mass at each tip, allows tuning of the primary torsion LNM such that it is close to the primary bending LNM. Perturbing the location of one mass relative to that of the other leads to veering between the eigenvalues of the bending and torsion LNMs. For a number of selected geometries in the region of veering, a nonlinear reduced order model (NLROM) is created and the nonlinear normal modes (NNMs) are used to describe the underlying nonlinear behaviour of the structure. The relationship between the 'closeness' of the eigenvalues and the nonlinear dynamic behaviour is demonstrated in the NNM backbone curves, and veering-like behaviour is observed. Finally, the forced and damped dynamics of the structure are predicted using several analytical and numerical tools and are compared to experimental measurements. As well as showing a good agreement between the predicted and measured responses, phenomena such as a 1:1 internal resonance and quasi-periodic behaviour are identified.

Keywords: Nonlinear Normal Modes, Nonlinear Beam, Closely-Spaced Modes of Vibration, Experimental Nonlinear Dynamics, Nonlinear Mode Veering

1 Introduction
An important consideration for structures operating in dynamic environments is the occurrence of closely spaced eigenvalues of the linear normal modes (LNMs) of vibration. This occurrence is particularly significant when eigenvalues become a function of operating conditions. For instance, closely-spaced eigenvalues can have a significant effect on the aero-elastic behaviour of wings since the 'closeness' of the eigenvalues affects the velocity at which the onset of flutter occurs [1]. Similarly, closely-spaced eigenvalues can strongly influence the dynamic response of a nonlinear system, and may result in strong internal resonances between the underlying LNMs and other nonlinear dynamic behaviour [2]. In this context, understanding the nonlinear interaction of LNMs, and how this interaction is influenced by the of the change of eigenvalues, is critical for many engineering structures.

In near-symmetric linear systems, the eigenvectors associated with closely-spaced eigenvalues can be highly sensitive to perturbations in the symmetry of the physical structure as described in [3]. Over larger perturbations in the symmetry, the phenomenon of mode veering can be observed [4, 5]; resulting in the separation of the eigenvalues and the correlation of the eigenvectors (e.g. off-axis terms in the modal assurance criterion [6] will appear). Examples of mode veering in the static perturbation of structures have been shown in a pressure vessel [7], cable dynamics [8, 9], a pre-stressed frame [10], and imperfect beams [11] with additional work connecting mode veering and mode localisation [12]. In contrast to the mode veering phenomenon, if a symmetry preserving change of geometry is applied to a structure, the closely-spaced eigenvalues will cross instead of veer [5], and no correlation will be observed between the eigenvectors.

It is well known that, for nonlinear systems, internal forces can cause an exchange of energy between nearly commensurate LNMs of vibration; termed internal, or auto-parametric, resonances. An in-depth line of work examining 1:2 resonances in a tuneable cantilever beam-mass system is detailed in [13], for example. For structures exhibiting closely-spaced eigenvalues, 1:1 internal resonances have been observed in the dynamics of symmetric systems with cubic nonlinearities [14] as well as stretched strings, beams, plates, and rotating disks as discussed by Nayfeh in [15], for example. Additionally, it has been shown that as physical parameters of stretched cables and symmetric shallow arches are changed, whilst preserving symmetry, a crossing occurs between uncorrelated natural frequencies (i.e. symmetric and anti-symmetric LNMs). At the point of crossing, a 1:1 internal resonance can be realised if the system of interest contains the proper orthogonality conditions discussed in [16]. Again, if the symmetry is broken through a change in physical parameters, the natural frequencies will veer instead of cross. Lacarbonara *et al* [11] investigated the nonlinear dynamics of an imperfect beam at veering, finding 1:1 internal resonances; however, only coupled motions of the modes of vibration were physically realized in the vicinity of veering contrary to the perfect beams investigated in [16], where the interaction between the linear modes was not activated.

The veering/crossing phenomena emphasises the importance of the inertial and stiffness distribution in structures with closely spaced eigenvalues. In dynamic linear systems, the inertial and stiffness properties of a structure is described using LNMs (i.e. eigenvalues and eigenvectors). A perturbation of either property directly affects the eigenvalues and eigenvectors, and veering/crossing can be observed in the correlation between the eigenvectors. In dynamic nonlinear systems, nonlinear normal modes (NNMs) of vibration [17] are used to describe the inertial and

stiffness properties of a structure. As a nonlinear system experiences a large amplitude of deformation, there is a potential for the effective mass and/or stiffness to change based on the mechanism of the nonlinearity. In continuous geometrically nonlinear systems, the change in effective mass and/or stiffness can be observed in the NNM backbone curves, i.e. the loci of NNM responses, as discussed in [18]. A deeper understanding of the dynamic motion is also be obtained by projecting the NNMs onto the underlying LNMs of vibration providing an indication of the activation of the nonlinear interaction [19, 20]. Nonlinearity often causes shifts in the response frequencies, which can have the effect of tuning the dynamic behaviour, leading to a nonlinear analogue of the linear veering behaviour.

This paper considers a clamped-clamped beam with movable masses, which allows the symmetry of the structure to be broken, and for the torsional inertia to be tuned. This not only enables the linear crossing and veering phenomena to be investigated, but also its influence on the nonlinear behaviour of the beam, which arises from dynamic tension effects. Nonlinear veering is demonstrated between closely-spaced eigenvalues of the fundamental bending and torsion LNMs of the beam. Veering between the fundamental LNMs is demonstrated using a full-order model in Abaqus® in section 2. In section 3, nonlinear interactions between two LNMs are identified using NNMs calculated from nonlinear reduced order models (NLROMs). The NLROMs used in this investigation are determined using static load cases and the geometric nonlinear capabilities of Abaqus® as described in [21, 22]. The resulting NNMs illustrate the undamped amplitude-dependent nonlinear behaviour between the two LNMs of interest and draw a connection back to the linear veering phenomena. Specifically, it is shown that, as amplitude increases, the initially bending-dominated NNM shifts in frequency more readily than that dominated by torsion. This results in the response frequency of the bending-dominated frequency approaches that of the torsion-dominated LNM. In turn, this leads to NNM responses composed of both bending and torsional components. This nonlinear veering-like behaviour requires both an asymmetry in the structure, and closely-spaced natural frequencies. In section 4, analytical and numerical tools are used to find the forced-damped dynamics of the NLROM. This reveals nonlinear phenomena such as 1:1 internal resonances as well as fold and torus bifurcations. Finally, in section 5, a comparison is made between the forced responses of the resulting NLROM and the experimentally measured response from a slow sine chirp to validate the behaviour found in the numerical study.

2 Structure and Model Description

2.1 Physical Description

The structure under consideration exhibits close natural frequencies between the first bending and first torsion LNMs, and consists of two beams joined in the middle as shown in Fig. 1a. The main beam is clamped at both ends and is joined in the middle to a cross-beam, which has concentrated masses attached at both ends. The concentrated masses are adjustable permitting the change of torsional inertia with limited influence on the bending inertia of the system (i.e. a change in L_1 and L_2 shown in Fig. 1a). A finite element model was created in Abaqus® to establish a high degree of freedom (DOF) linear model. A total of 288 B31 beam elements, (6 DOFs at each node [22]) were used to discretise the cross section of each beam resulting in a total of 1734 DOF. The length, width, and thickness of the main beam are 1000mm, 12mm, and 6mm, respectively, and the length and diameter of the cross-beam are 410mm and 12mm respectively. The diameter and width of the concentrated masses are 38mm and 24mm, respectively. The final experimental setup is shown in Fig. 1b.

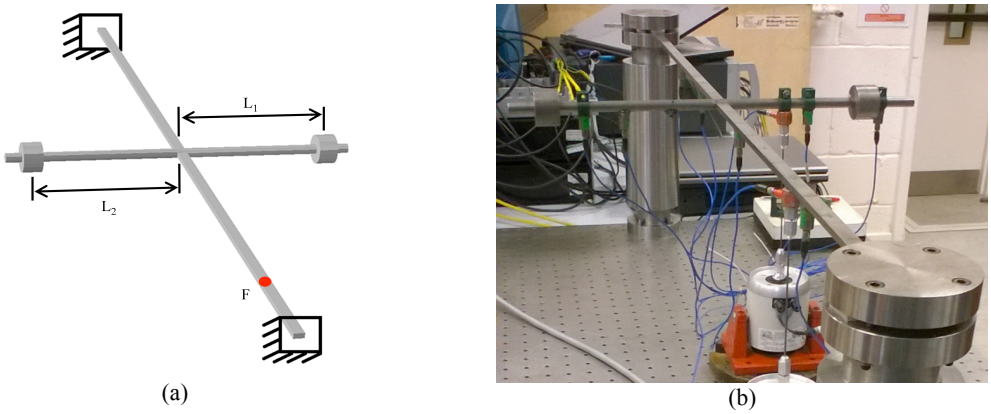

(a) (b)

Figure 1: Clamped-clamped cross-beam, a) Abaqus model, b) actual structure

It has been discussed that the perturbation of physical properties of a structure with closely-spaced natural frequencies will cause the eigenvalues to veer (corresponding to a rapid change in the eigenvectors) or cross. This effect is explored by modifying the mass distribution of the cross-beam through changing the location of the tip masses (L_1 and L_2), and computing the eigenvalues and eigenvectors of the cross-beam. The location of the concentrated masses at the point of veering/crossing (L_1=$L_{1,0}$ and L_2=$L_{2,0}$) is determined by identifying the smallest allowable spacing in the region of veering/crossing between the fundamental bending and torsion eigenvalue. Two primary cases are considered: the first is the symmetric case where $L_{S1,0} = L_{S2,0} = 182.5$mm, and the second is the asymmetric case where $L_{A1,0} = 187.0$ and $L_{A2,0} = 0.95\ L_{A1,0} = 177.7$mm. Additionally, the values of $L_{S1,0}$ and $L_{A1,0}$ are perturbed +/-5mm (ΔL_1 = +/-5mm) to further

explore nonlinear interactions in the veering/crossing region. Throughout this and the following sections, LNM 1 refers to the mode with the lowest eigenvalue and LNM 2 refers to the mode with the second lowest eigenvalue, which is consistent throughout much of the literature.

2.2 Nonlinear Modelling

The influence of nonlinear behaviour due to dynamic tension effects in the main beam is now addressed. Although the Abaqus® model is relatively small, performing nonlinear dynamic analysis is computationally expensive. Instead, we consider the dynamics of the structure in terms of a reduced set of LNMs, capturing any modal interactions between these modes, that result from the nonlinear behaviour of the structure. A set of two-mode, nonlinear reduced order models (NLROMs) were created, consisting of the first bending- and first torsion-dominated linear modes.
The nonlinear behaviour of these modes was captured using the implicit condensation and expansion method (ICE) – see [21] and references therein for an in-depth description of the ICE method. The nonlinear stiffening due to axial stretching at large amplitudes of deformation are implicitly accounted for using nonlinear static solutions in Abaqus®. For specified levels of applied modal forces, the resulting deformation is decomposed onto the preselected modal basis for the NLROM, and the nonlinear stiffness coefficients are determined by identifying coefficients of the restoring force and modal displacement relationship. The ICE method produces an N DOF system of equations in the modal domain as

$$\ddot{\mathbf{q}} + \mathbf{\Lambda}\mathbf{q} + \mathbf{N}_q(\mathbf{q}) = 0 \tag{1}$$

Since this work focuses on a two DOF representation of the interaction between the fundamental bending and torsion LNM of the clamped-clamped crossbeam, the terms in Eqn. (1) become

$$\mathbf{q} = \begin{bmatrix} q_1 \\ q_2 \end{bmatrix}, \qquad \mathbf{\Lambda} = \begin{bmatrix} \omega_{n1}^2 & 0 \\ 0 & \omega_{n2}^2 \end{bmatrix},$$
$$\mathbf{N}_q(q) = \begin{pmatrix} \alpha_1 q_1^2 + 2\alpha_2 q_1 q_2 + \alpha_3 q_2^2 + \gamma_1 q_1^3 + 3\gamma_2 q_1^2 q_2 + \gamma_3 q_1 q_2^2 + \gamma_4 q_2^3 \\ \alpha_2 q_1^2 + 2\alpha_3 q_1 q_2 + \alpha_4 q_2^2 + \gamma_2 q_1^3 + \gamma_3 q_1^2 q_2 + 3\gamma_4 q_1 q_2^2 + \gamma_5 q_2^3 \end{pmatrix} \tag{2}$$

where q_i, and ω_{ni} represent the displacement and natural frequency of the i^{th} LNM, respectively. Additionally, α_i and γ_i are nonlinear parameters of a generalised cubic function which are determined using the ICE method [21], resulting in quadratic and cubic terms. As discussed in [21], the number of nonlinear parameters is reduced by recognising a linear dependency between certain nonlinear terms, as reflected in Eqn. (2). For reference, the parameter values of the symmetric ($L_{S1,-5}$) and asymmetric ($L_{A1,-5}$) models when ΔL_1 = -5 mm are shown in Tab. 1.

Table 1: Nonlinear Parameters for Symmetric and Asymmetric System where ΔL = -5 mm.

Model	ω_{n1}	ω_{n2}	α_1	α_2	α_3	α_4	γ_1	γ_2	γ_3	γ_4	γ_5
$L_{S1,-5}$	101.938	105.859	-362.117	-0.749	2.653	-0.147	1.509×10^{8}	-90.968	2.997×10^{5}	0.653	2.558×10^{5}
$L_{A1,-5}$	101.744	104.634	179.984	15.126	0.406	-0.0985	1.325×10^{8}	3.438×10^{7}	2.708×10^{7}	2.332×10^{6}	8.535×10^{5}

2.3 Analytical Analysis

NLROMs are used to find the backbone curves, or frequency-amplitude relationships composed of the NNMs. The backbone curves of the two-mode NLROM can be easily analysed using the harmonic balance method [23]. To first-order accuracy, this method relies on the assumption that the displacement of any mode may be approximated using a single harmonic. As the two modes of interest here are expected to have a fundamentally activated nonlinear interaction (1:1), it is assumed that the motion of the i^{th} mode takes the form

$$q_i \approx u_i = U_i \cos(\Omega t - \phi_i) = \frac{U_i}{2} e^{+\mathrm{j}(\Omega t - \phi_i)} + \frac{U_i}{2} e^{-\mathrm{j}(\Omega t - \phi_i)} \tag{3}$$

where U_i, ϕ_i are the amplitude and phase of u_i, and Ω is the response frequency. Note that u_i denotes the single-harmonic approximation to q_i. The next step of the harmonic balance method involves substituting the assumed solution, Eq. (3), into the equation of motion, Eq. (1). After expanding the resulting expressions, the terms that are *non-resonant*, i.e. those that do not resonate at frequency Ω, are removed. This is a simple, but algebraically involved process and, as such, will be demonstrated using the single term, $\gamma_3 q_1^2 q_2$. Substituting Eq. (3) into this term leads to

$$\gamma_3 q_1^2 q_2 = \frac{\gamma_3}{8} U_1^2 U_2 \left(e^{+\mathrm{j}(3\Omega t - 2\phi_1 - \phi_2)} + 2e^{+\mathrm{j}(\Omega t - \phi_2)} + e^{-\mathrm{j}(\Omega t - 2\phi_1 + \phi_2)} + e^{+\mathrm{j}(\Omega t - 2\phi_1 + \phi_2)} + 2e^{-\mathrm{j}(\Omega t - \phi_2)} + e^{-\mathrm{j}(3\Omega t - 2\phi_1 - \phi_2)} \right) \tag{4}$$

It can be seen that the first and last terms of Eq. (4) resonate at a frequency of 3Ω and hence are considered non-resonant and are neglected. Applying this procedure to all terms in the equations of motion, Eq. (1), leads to

$$\begin{aligned}
&\left[\left(\omega_{n1}^2-\Omega^2\right)U_1+\frac{3\gamma_1}{4}\mathrm{U}_1^3+\frac{3\gamma_2}{4}\mathrm{U}_1^2\mathrm{U}_2\left(\mathrm{e}^{-\mathrm{j}\phi_d}+2\mathrm{e}^{+\mathrm{j}\phi_d}\right)+\frac{\gamma_3}{4}\mathrm{U}_1\mathrm{U}_2^2\left(\mathrm{e}^{+\mathrm{j}2\phi_d}+2\right)+\frac{3\gamma_4}{4}\mathrm{U}_2^3\mathrm{e}^{+\mathrm{j}\phi_d}\right]\mathrm{e}^{+\mathrm{j}(\Omega t-\phi_1)}+\mathrm{CC.}=0\\
&\left[\left(\omega_{n2}^2-\Omega^2\right)U_2+\frac{3\gamma_2}{4}\mathrm{U}_1^3\mathrm{e}^{-\mathrm{j}\phi_d}+\frac{\gamma_3}{4}\mathrm{U}_1^2\mathrm{U}_2\left(\mathrm{e}^{-\mathrm{j}2\phi_d}+2\right)+\frac{3\gamma_4}{4}\mathrm{U}_1\mathrm{U}_2^2\left(\mathrm{e}^{+\mathrm{j}\phi_d}+2\mathrm{e}^{-\mathrm{j}\phi_d}\right)+\frac{3\gamma_5}{4}\mathrm{U}_2^3\right]\mathrm{e}^{+\mathrm{j}(\Omega t-\phi_2)}+\mathrm{CC.}=0
\end{aligned} \tag{5}$$

where $\phi_d = \phi_1 - \phi_2$ and CC. denotes the complex conjugate terms. Note that the quadratic terms are non-resonant. The terms in the square brackets in Eq. (5) may be equated to zero, to give

$$\begin{aligned}
&\left(\omega_{n1}^2-\Omega^2\right)U_1+\frac{3\gamma_1}{4}\mathrm{U}_1^3+\frac{3\gamma_2}{4}\mathrm{U}_1^2\mathrm{U}_2\left(\mathrm{e}^{-\mathrm{j}\phi_d}+2\mathrm{e}^{+\mathrm{j}\phi_d}\right)+\frac{\gamma_3}{4}\mathrm{U}_1\mathrm{U}_2^2\left(\mathrm{e}^{+\mathrm{j}2\phi_d}+2\right)+\frac{3\gamma_4}{4}\mathrm{U}_2^3\mathrm{e}^{+\mathrm{j}\phi_d}=0\\
&\left(\omega_{n2}^2-\Omega^2\right)U_2+\frac{3\gamma_2}{4}\mathrm{U}_1^3\mathrm{e}^{-\mathrm{j}\phi_d}+\frac{\gamma_3}{4}\mathrm{U}_1^2\mathrm{U}_2\left(\mathrm{e}^{-\mathrm{j}2\phi_d}+2\right)+\frac{3\gamma_4}{4}\mathrm{U}_1\mathrm{U}_2^2\left(\mathrm{e}^{+\mathrm{j}\phi_d}+2\mathrm{e}^{-\mathrm{j}\phi_d}\right)+\frac{3\gamma_5}{4}\mathrm{U}_2^3=0
\end{aligned} \tag{6}$$

To solve Eq. (6), we first consider the imaginary components

$$\begin{aligned}
&\frac{3\gamma_2}{4}\mathrm{U}_1^2\mathrm{U}_2\sin(\phi_d)+\frac{\gamma_3}{4}\mathrm{U}_1\mathrm{U}_2^2\sin(2\phi_d)+\frac{3\gamma_4}{4}\mathrm{U}_2^3\sin(\phi_d)=0\\
&-\frac{3\gamma_2}{4}\mathrm{U}_1^3\sin(\phi_d)-\frac{\gamma_3}{4}\mathrm{U}_1^2\mathrm{U}_2\sin(2\phi_d)-\frac{3\gamma_4}{4}\mathrm{U}_1\mathrm{U}_2^2\sin(\phi_d)=0
\end{aligned} \tag{7}$$

which both lead to the condition

$$\left[3\gamma_2\mathrm{U}_1^2+2\gamma_3\mathrm{U}_1\mathrm{U}_2\cos(\phi_d)+3\gamma_4\mathrm{U}_2^2\right]\sin(\phi_d)=0 \tag{8}$$

This may be satisfied by setting $\sin(\phi_d) = 0$ (i.e. $\phi_1 - \phi_2 = 0$ or $\phi_1 - \phi_2 = \pi$). Using this, the real parts of Eq. (6) give

$$\begin{aligned}
\Omega^2&=\omega_{n1}^2+\frac{1}{4}\left[3\gamma_1U_1^2+p9\gamma_2U_1U_2+3\gamma_3U_2^2+p3\gamma_4U_1^{-1}U_2^3\right]\\
\Omega^2&=\omega_{n2}^2+\frac{1}{4}\left[p3\gamma_2U_1^3U_2^{-1}+3\gamma_3U_1^2+p9\gamma_4U_1U_2+3\gamma_5U_2^2\right]
\end{aligned} \tag{9}$$

where the variable p is defined as

$$p=\cos(\phi_1-\phi_2)=\begin{cases}+1 & \text{when}\quad \phi_1-\phi_2=0\\ -1 & \text{when}\quad \phi_1-\phi_2=\pi\end{cases} \tag{10}$$

where $p = +1$ and $p = -1$ represent the cases where the two underlying linear modes are and in anti-phase respectively. Finally, eliminating Ω^2 from Eqs. 9 gives the amplitude relationship

$$\left[p3\gamma_2\right]U_1^4+\left[3(\gamma_3-\gamma_1)U_2\right]U_1^3+\left[p3(3\gamma_4-3\gamma_2)U_2^2\right]U_1^2+\left[4\left(\omega_{n2}^2-\omega_{n1}^2\right)U_2+3(\gamma_5-\gamma_3)U_2^3\right]U_1-\left[p3\gamma_4U_2^4\right]=0 \tag{11}$$

This expression may be used, alongside Eq. (9), to compute the NNM backbone curves of this system in terms of amplitude of the fundamental components, U_1 and U_2, and the fundamental response frequency Ω.

In the following section, response frequency-energy plots (FEPs) will be presented. In the FEPs, the energy is calculated from the amplitudes of the fundamental components using

$$\text{Energy}=\int_0^u F(u)=\int_0^u \Lambda u+N_u(u)du \tag{12}$$

where $N_u(u)$ represents the resonant terms in $N_q(u)$, from Eq. (2).

2.4 NLROM Verification with NNMs

It is important to remember that the analysis above is based upon a low order representation of a continuous structure, and so its validity is now assessed. Due to the computational expense of the high-order finite element model, one case from each of the symmetric and asymmetric configurations is compared with results obtained using the NLROMs. To further reduce the computational cost of finding the backbone curves using the high-order model, the continuation procedure outlined in [24, 25] is employed. Using symmetric ($L_{S1,-5}$) and asymmetric ($L_{A1,-5}$) cases, where ΔL_1 = -5mm, the NNMs for the symmetric and asymmetric case are computed using both the full- and reduced-order models and compared in Fig. 2. The physical interpretation of these NNMs is discussed later, but their presentation here demonstrates the fit of the NLROM when compared to the full-order model – the NLROMs predict the bending-dominated responses to within 1% error for the frequency range of interest; however, as the torsion dominated motion reaches higher energies, the NLROM begins to diverge from the predicted solution. This difference is likely to be due to nonlinear inertia effects of the tip masses, or to the effective shortening of the beam due to torsion, which leads to a poor fit of the NLROM at high energies. As this divergence begins near the material elastic limit, it is concluded that the NLROM produces an accurate representation of the system in the dynamic range achievable in the experimental setup.

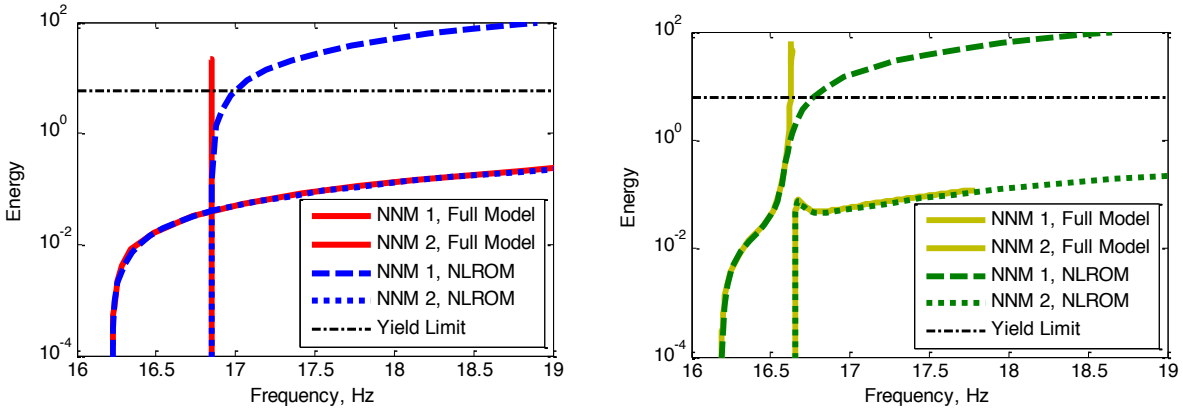

Figure 2: Nonlinear normal mode comparison of the full and nonlinear reduced order models for the (a) symmetric case ($L_{S1,-5}$) and (b) asymmetric case ($L_{A1,-5}$)

3 Veering

3.1 Linear Normal Mode Veering

The eigenvalues and eigenvectors presented in this section were found for the high-order model using the Abaqus® Lanczos solver, as here we are considering veering within the linear regime. When the structure is symmetric, the crossing point occurs at $L_1 = L_2$ = 182.5mm, denoted $L_{S1,0}$. Due to the discretisation of the system, the exact crossing point cannot be identified; however, the crossing point can be isolated to within a frequency spacing of 0.006Hz. As illustrated in Fig. 3, an increase of $L_1 = L_{S1,0} + \Delta L_1$, with ΔL_1 = 5mm and $L_1 = L_2$, results in a torsion LNM at 15.93Hz and a bending LNM at 16.20Hz. Alternatively, a decrease in L_1, with ΔL_1 = -5mm results in a bending mode at 16.21Hz and a torsion LNM at 16.53Hz. Using self-MAC values to quantify the independent nature of the eigenvectors for these symmetric configurations, it can be seen that there is no dependence and the LNMs will cross. The instance of eigenvalue crossing for the symmetric system is shown in Fig. 3b (in blue) where the eigenvalue is considered as the length is altered. As the change in length is increased from -5mm to 0mm, the LNM 1 (bending mode) approaches LNM 2 (torsion mode). At the point of crossing, the torsional mode becomes LNM 1 and the bending mode becomes LNM 2 with no veering observed.

If the symmetry is broken by setting $L_1 \neq L_2$, the torsion and bending dominated modes deviate from pure bending or pure torsion. As the torsional inertia is modified to change the spacing of the eigenvalues, LNM veering rather than crossing is observed. The case when $L_2 = 0.95\ L_1$, is also shown in Fig. 3, where veering occurs at L_1 = 187.0mm, denoted $L_{A1,0}$. The eigenvectors, shown in Fig. 3a, appear as a summation of the uncorrelated bending- and torsion-LNMs (i.e. bending and torsion are equally represented in the deformation of the beam). As L_1 is increased +5mm ($L_{A1,+5}$), the eigenvectors become almost completely orthogonal for both cases where the torsion dominated mode is LNM 1 and the bending dominated mode is LNM 2. Alternatively, as L_1 is decreased -5mm ($L_{A1,-5}$), the eigenvectors become more orthogonal, with LNM 1 being dominated by bending and LMN 2 by torsion. Figure 3b, which shows the relationship between natural frequency against the change in length, demonstrates the veering (green lines) for this asymmetric case. Again, an examination of the self-MAC provides quantification for the correlation between the two modes of interest. As the change in length is increased from -10mm to 0mm, both instances demonstrate a limit of 'closeness' in the eigenvalues as the interaction between the LNMs is activated. As the change in length is increased from 0 to 10mm, the opposite behaviour is demonstrated with the eigenvector switched. The case of linear veering have

also been experimentally examined in [8], so the remainder of this paper will focus on the nonlinear behaviour observed between these two modes.

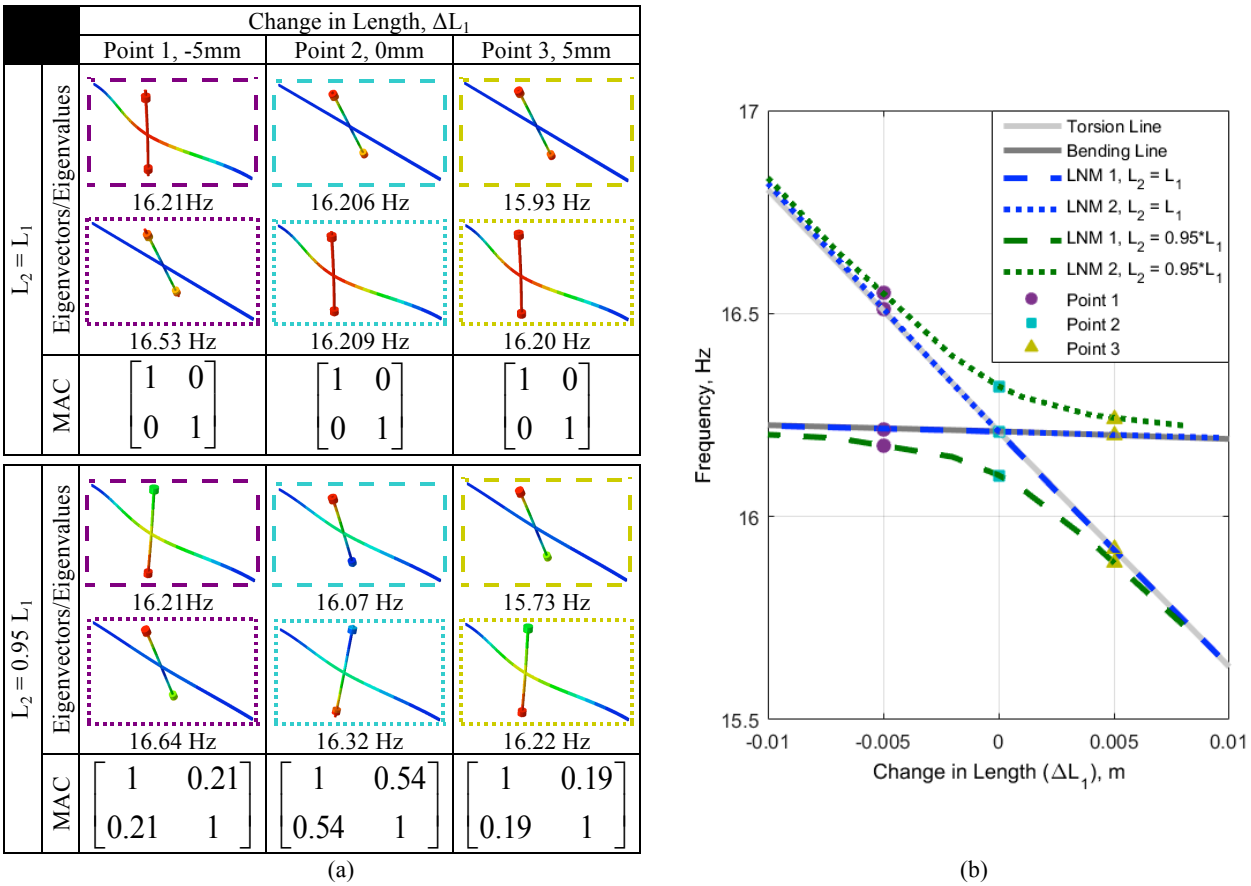

Figure 3: Description of linear veering/crossing for the first (— —) and the second (▪ ▪ ▪ ▪) linear normal modes of vibration for the symmetric (blue) and asymmetric (green) configurations of the tip masses' locations, a) changes in mode shapes through veering or crossing, b) change in length, eigenvalue vs. ΔL_1

3.2 Nonlinear Normal Modes

Mode veering due to changes in mass distribution has been discussed and shown to provide interesting behaviour between the purely bending and torsion eigenvectors of the structure. At large deformation amplitudes, axial stretching increases the effective stiffness, and hence the natural frequency, of the bending mode, while minimal change is observed in the torsional mode. This change of one frequency of vibration while the other remains the same provides a potential for nonlinear veering as the two frequencies coalesce. NNMs calculated using the harmonic balance method [23] at different ΔL_1 values detail this nonlinear veering or crossing phenomenon. In the following discussion, the NNMs are presented by considering how the average and the difference in the tip displacements of the cross-beam change with frequency. These projections give an indication of whether the structural deformation is primarily bending or torsion. Using the predicted NNM deformation, the peak stress was calculated in Abaqus® and the cyclic yield limit was identified using [26], which is indicated in the following figures with a (*).

Beginning with the symmetric case, $L_1 = L_2$, the NNMs are computed for three geometries within the range of crossing (ΔL_1 = -10, 0, and 10 mm) and are shown in Fig. 4a and 4b. The NNMs computed along the torsion line result in a large tip difference (i.e. remain primarily torsion), while those computed along the bending line result in a large tip mean (i.e. remain primarily bending). In both sets of NNMs a spring hardening effect is observed due to increased effective stiffness for both modes, as predicted by the NLROMs; however, the hardening is more pronounced in the bending dominated NNMs. As the response is pushed into the nonlinear region, the two modes of interest act as nonlinear continuations of their linear counterparts, with no nonlinear interaction between the two modes observed. Note that for the case where the natural frequency of the bending mode is lower than the torsion mode, the NNMs appear to cross.

Now consider the asymmetric case where $L_2 = 0.95\ L_1$. As shown in section 3.1, the eigenvectors in all three configurations have off-axis values in their self-MAC due to the asymmetry introduced to the physical structure by the difference in location of the tip masses. The NNMs for several configurations are calculated in the region of veering identified previously and are shown in Fig. 4c and 4d. The tip difference and tip mean show strong contributions in both NNMs, showing that the two modes are a combination of bending and torsion. NNM 1 shows a sharp increase of tip difference with increasing fundamental frequency, indicating a transition to a torsionally-dominant motion. NNM 2 shows a similar sharp transition in the tip difference as the fundamental frequency of vibration is increased and ΔL_1 becomes negative. This sharp transition is reduced as ΔL_1 becomes positive.

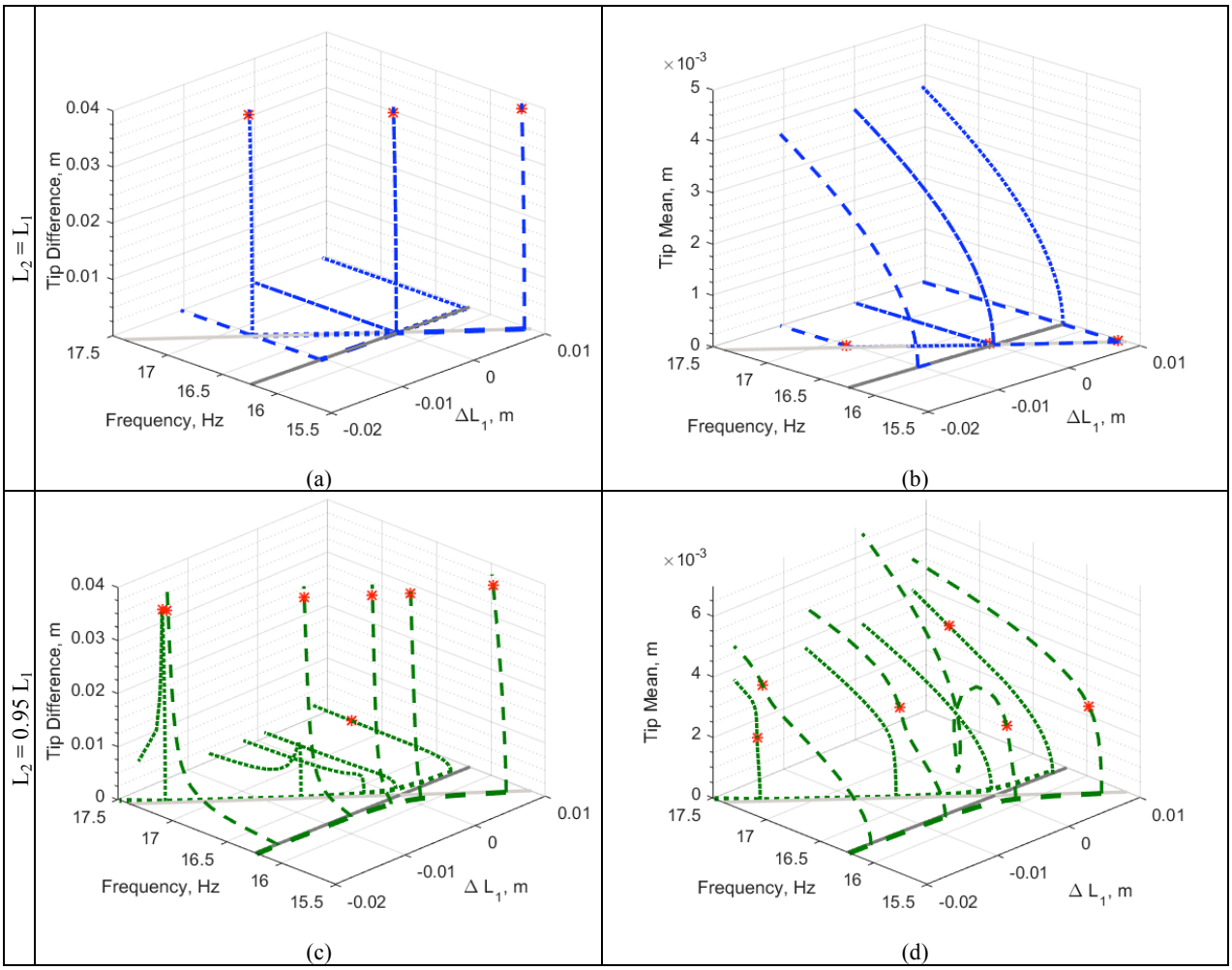

Figure 4: Magnitude of tip difference based on computed nonlinear normal modes for the symmetric (a & b) and asymmetric (c & d) configurations. The NNMs are identified as starting in the first (— —) or the second (▪ ▪ ▪ ▪) LNMs of vibration. The cyclic yield predicted by the stress distribution from the NNM deformation is calculated using [26] and shown as (*).

In both the symmetric and the asymmetric cases, when the torsion LNM has a lower eigenvalue than the bending LNM of vibration, no veering/crossing is observed between the NNMs since the nonlinear stiffening affects the bending-dominated NNM before the torsion-dominated NNM. A nonlinear crossing/veering phenomonon can be observed in Fig. 4 for negative values of ΔL_1. In the frequency region of interest, the torsion motion hits the elastic material limit before the bending motion as indicated in Fig. 4a and 4c requiring further consideration in the structural design. For the remainder of this investigation, ΔL_1 = -5mm is selected for the symmetric ($L_{S1,-5}$) and asymmetric ($L_{A1,-5}$) cases so the nonlinear veering phenomona can be explored within the predicted elastic limit of the system.

For completeness, the deformation shapes and frequency-energy plot (FEP) of the symmetric case ($L_{S1,-5}$) for ΔL_1 = –5mm are shown in Figs. 5a and 5b. At low response energy (i.e. approximately linear response at Point 1) the deformation of NNM 1 and NNM 2 match the LNM 1 and LNM 2 eigenvectors predicted for the symmetric model shown in Fig. 3, as expected. At the point of crossing (Point 2), the dominant motion of the response for NNM 1 and NNM 2 switch as the natural frequency of the bending mode increases past that of the torsional one. As with the eigenvectors of the symmetric case at linear crossing, the predicted deformation of each NNM at nonlinear crossing show no correlation.

The corresponding plots for the asymmetric case ($L_{A1,-5}$) are shown in Figs. 5c and 5d. Again, at a low response energy (i.e. linear response at Point 1) the NNM 1 and NNM 2 deformation shapes match the LNM 1 and LNM 2 eigenvectors predicted for the asymmetric model shown in Fig. 3, as expected. At the point of veering (Point 2), the predicted shapes become combinations of the separate bending and torsion motions. Similar to the veering observed for the change in mass distribution of the linear structure, the fundamental frequency of the NNMs approach each other, but do not cross. At higher response energies (Point 3), the NNM shapes are now flipped so the torsion dominated shape is at a lower frequency than the bending dominated shape.

In this section it has been shown that nonlinearities can lead to a veering-like behaviour. In the following section we will consider how this influences the forced response.

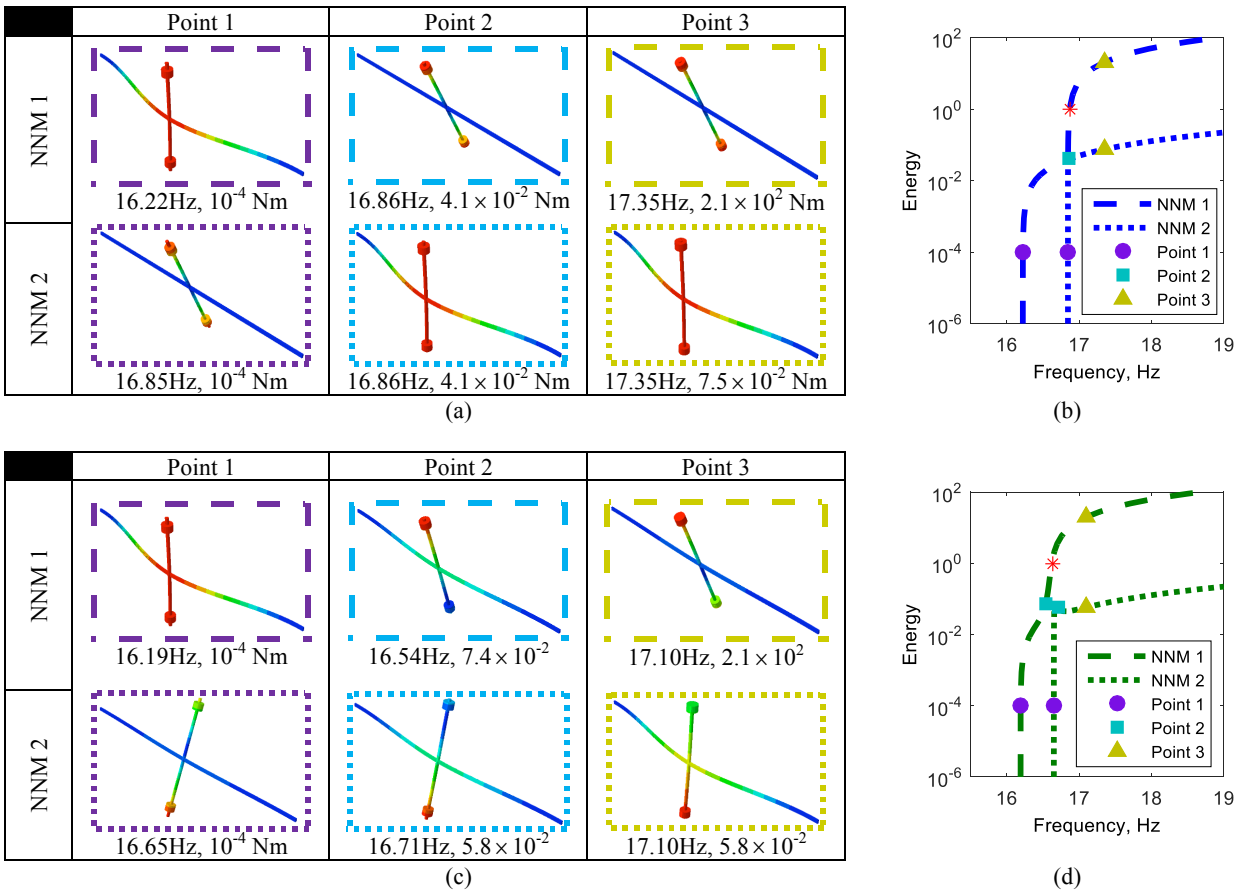

Figure 5: Detail of nonlinear veering/crossing phenomina of NNM 1 (— —) and NNM 2 (▪ ▪ ▪ ▪) for the symmetric (a & b) and asymmetric (c & d) configuration with ΔL_1 = -5mm in both cases. Detailed deformation shapes (a & c) are presented at specific point along the frequency-energy plot (b & d). The cyclic yield predicted by the stress distribution from the NNM deformation is calculated using [26] and shown as (*).

4 Nonlinear Forced Response

Although much insight into the dynamic response of a structure is gained using LNMs and backbone curves, both are limited to the unforced, undamped equations of motion. It is therefore important to also examine the forced and damped response of the structure around the modes of interest. Since the NLROM NNMs have been shown to match the full-order model NNMs, the NLROMs are now used to explore the forced and damped response of the structure. It is beneficial to make a connection between the NNMs previously discussed and the forced response at resonance of the structure using the energy transfer method. This method, which was proposed in [12] and later developed in [20], enables the development of analytical expressions describing the *resonant crossing points* (i.e. the points at which the forced response crosses the NNMs at resonance). The approach used here is similar to that presented in [27], where it is used to predict the existence of isolas in the forced responses.

4.1 Energy Transfer Analysis

Energy transfer analysis relies on the observation that, for any system exhibiting a steady-state periodic response, the net energy transfer out of the system (i.e. out of both modes for the NLROM) over one period must be zero. For the cross-beam considered here, energy may only be transferred out of the system due to the external sinusoidal forcing and viscous modal damping. Therefore, the net energy transfer out of the i^{th} linear mode due to the forcing and damping terms over one period of motion may be written as

$$E_i = \int_0^T \left[2\zeta_i \omega_{ni} \dot{q}_i - P_i F \cos(\Omega t)\right] \dot{q}_i dt \tag{13}$$

where $T = 2\pi\Omega^{-1}$ is the period of the response. Additionally, ζ_i is the i^{th} modal damping coefficient, F is the amplitude of forcing, and P_i is the i^{th} modal force calculated from the projection of the single point excitation into the modal domain. Using the approximation $q_i = u_i$, along with the assumed solution for u_i given in Eq. (3), Eq. (13) may be written as

$$E_i = \pi U_i \left[2\zeta_i \omega_{ni} \dot{q}_i - P_i F \cos(\Omega t) \right] \tag{14}$$

Considering the two-mode model, the net energy transfer out of a system over one period of motion may be expressed as $E_1 + E_2$. For any steady-state response, this net energy transfer must be zero, i.e. $E_1 + E_2 = 0$, which, using Eq. (14), gives

$$F = \frac{2\Omega\left(\zeta_1 \omega_{n1} U_1^2 + \zeta_2 \omega_{n2} U_2^2\right)}{P_1 U_1 \sin(\phi_1) + P_2 U_2 \sin(\phi_2)} \tag{15}$$

This expression requires the phases ϕ_1 and ϕ_2 to be known; however, on the backbone curves, only the *relationship* between the phases is known, and so Eq. (15) cannot be used directly. Instead, the assumption that the forcing is *in-quadrature* with the responses must be used, as discussed in [20]. This assumption allows the approximation $\phi_i = \pm\pi/2$ to be substituted into Eq. (15) leading to

$$F = \frac{2\Omega\left(\zeta_1 \omega_{n1} U_1^2 + \zeta_2 \omega_{n2} U_2^2\right)}{\left| P_1 U_1 + p P_2 U_2 \right|} \tag{16}$$

where p is defined in Eq. (10). The energy transfer analysis also relies on the assumption that the forced response of a structure crosses the NNM backbone curve precisely, such that they share a solution. As such, if the solution for a point on a backbone curve – in terms of Ω, U_1, and U_2 – is substituted into Eq. (16), it may be used to determine the forcing amplitude, F, that is required to cross that point on the NNM backbone curve at resonance. However, it is found that not all predicted points are met by the forced response, even when the forcing amplitude is that given in Eq. (16). This demonstrates that there are points on a backbone curve that cannot be reached by a forced response at resonance. The mechanism underpinning this, and an approach for computing a metric for assessing whether or not a point may be reached is now discussed.

In [20], a method for estimating the relative accuracy of a resonant crossing point prediction was introduced. This relies on the observation that, for a steady-state response of a system, the net energy transfer into, or out-of, *any mode* must be zero over a timer period T. This constraint is in addition to the requirement discussed previously, that the energy transfer for the entire system must be zero. In order to achieve zero modal energy transfer, the phase difference between the modes must precisely equal to the phase difference on the backbone curve (i.e. $\phi = \phi_1 - \phi_2 = 0$). Conversely, a phase difference that is not equal to that on the backbone curve will lead to energy transfer between the modes. As such, if the required energy transfer is known, the phase difference that will allow this can be computed. This phase-difference provides a metric for estimating the relative accuracy of the resonant crossing points.

Considering the first mode of the cross-beam, energy transfer may occur due to the forcing and damping terms, as considered previously, but also due to energy transfer into the second mode. From the first equation in Eq. (6), this energy transfer may be written as

$$E_{12} = \int_0^T \left[3\gamma_2 \left(2u_{p1} u_{m1} u_2 + u_{m1}^2 u_{p2} + u_{p1}^2 u_{m2} \right) + \gamma_3 \left(u_{p1} u_{m2}^2 + u_{m1} u_{p2}^2 + 2u_1 u_{p2} u_{m2} \right) + 3\gamma_4 u_{p2} u_{m2} u_2 \right] \dot{u}_1 dt \tag{17}$$

where, from Eq. (3)

$$u_{pi} = \frac{U_i}{2} \mathrm{e}^{+\mathrm{j}(\Omega t - \phi_i)}, \qquad \text{and} \qquad u_{mi} = \frac{U_i}{2} \mathrm{e}^{-\mathrm{j}(\Omega t - \phi_i)} \tag{18}$$

Using Eq. (17) and evaluating the integral, this may be computed as

$$E_{12} = \frac{\pi U_1 U_2}{4} \left[3\gamma_2 U_1^2 + 2\gamma_3 U_1 U_2 \cos(\phi_1 - \phi_2) + 3\gamma_4 U_2^2 \right] \sin(\phi_1 - \phi_2) \tag{19}$$

Using Eq. (14) and equating the total net energy transfer out of the first mode to zero leads to the expression

$$\sin(\phi_1 - \phi_2) = \frac{4\left[P_1 F \sin(\phi_1) - 2\zeta_1 \omega_{n1} \Omega U_1\right]}{U_2\left[3\gamma_2 U_1^2 + 2\gamma_3 U_1 U_2 \cos(\phi_1 - \phi_2) + 3\gamma_4 U_2^2\right]} \tag{20}$$

which allows the phase-difference, required for zero net energy transfer from the first mode, to be computed. However, $\sin(\phi_1)$, must be estimated. As ϕ_1 is close to $\pm\pi/2$ (i.e. the response is close to quadrature), we approximate $\sin(\phi_1) = \pm 1$. To assess the sign of this relationship, consider Eq. (15), where it can be seen that $P_1U_1\sin(\phi_1) + P_2U_2\sin(\phi_2) > 0$ or $(P_1U_1 + pP_2U_2)\sin(\phi_1) > 0$. Assuming $P_1 > 0$ and $P_2 > 0$, in the case where $p = +1$ then $\sin(\phi_1) = 1$. When using p = -1, the sign of $\sin(\phi_1)$ depends on the excitation and response; if $(P_1U_1)(P_2U_2)^{-1} > 1$ then $\sin(\phi_1) = 1$ and if $(P_1U_1)(P_2U_2)^{-1} < 1$ $\sin(\phi_1) = 1$. Using these relationships with Eq. (**Error! Reference source not found.**), the phase difference may be estimated. This phase difference provides an approximate metric for the validity of the resonant crossing points. If the phase difference is very small (i.e. $0 < \phi_1 - \phi_2 << \pi/2$), it suggests that the forcing energy input to both modes is near correct for that particular point, and the system is able to correct for any error with a small change in phase – as such it may be assumed that the resonance is close to the backbone curve. Conversely, if the phase difference is near to $\pi/2$, or if no real solution exits for Eq. (**Error! Reference source not found.**), it suggests that the resonance is far from the predicted resonant crossing point on the backbone curve.

4.2 Resonant Crossing Points

The resonant crossing points can now be considered for the symmetric and asymmetric configurations with ΔL = -5mm. To match the experimental setup, the damping values used for the resonant crossing point analysis are determined from multi-input and multi-output modal testing and the Algorithm for Mode Isolation [28]. The modal forcing characteristics used for this analysis represent a single point excitation 10 cm from the clamp as seen in Fig. 1a.

The validity of the resonant crossing points for the symmetric and asymmetric system is demonstrated in Figs. 6a and 6b, respectively. The phase difference between the underlying modes, calculated using Eq. (**Error! Reference source not found.**), gives a measure of accuracy, with a phase close to zero being an accurate point. Since no modal interaction is observed in the symmetric case (Fig. 6a), the mechanism of energy transfer, which causes some points to be inaccurate, does not exist. From Fig. 6b, the crossing point calculated for NNM 1 at 5N is shown to be more accurate than the crossing point at 3.5N. For NNM 2, only one point for the 5.0N forcing level is shown to be accurate, while two are accurate for the 3.5N forcing level. It is interesting to note that the two crossing points predicted for the 3.5N level indicate an isolated forced response [27], while the single crossing point for the 5.0N case signifies the disappearance of this isolated forced response. The results of this analysis suggests the forcing case at 5.0N provides the best potential for comparison with experiment through the region of veering without the need for a complicated control algorithm to measure the isola [29].

Simulation of the forced response using numerical continuation techniques provides a further check of the validity of the resonant crossing points. For the symmetric system (Figs. 6c and e), the resonant crossing points and the forced response match well and show a dynamic behaviour dominated by LNM 1 (Fig. 6c). In the asymmetric case (Fig. 6d and f), the modal interaction is more apparent. The resonant crossing points for NNM 1 show good agreement for the interaction between LNM 1 (Fig. 6d) and LNM 2 (Fig. 6f) and resembles a typical stiffening behaviour. For NNM 2, the forced response shows more complicated behaviour, but the accurate resonant crossing points are shown to match the forced response well. An examination of the Floquet exponents from the forced response as calculated in FCont [30] reveals unstable regions in dynamic response corresponding to fold bifurcations and torus bifurcations (light red). The isolated forced response at the 3.5N forcing level is shown to relate to an unstable quasi-periodic (QP) exchange of energy between LNM 1 and LNM 2 due to a torus bifurcation. A similar QP solution is observed when the forcing is increased to 5.0N; however, the unstable isolated forced response branch becomes attached to the stable forced response branch. This QP region of the dynamic response directly relates to the NNM veering region previously identified. With an input forcing level of 5.0N, the QP region lies in between two periodic regions of the forced response allowing for comparison with an experimental sine sweep as explored in section 5.

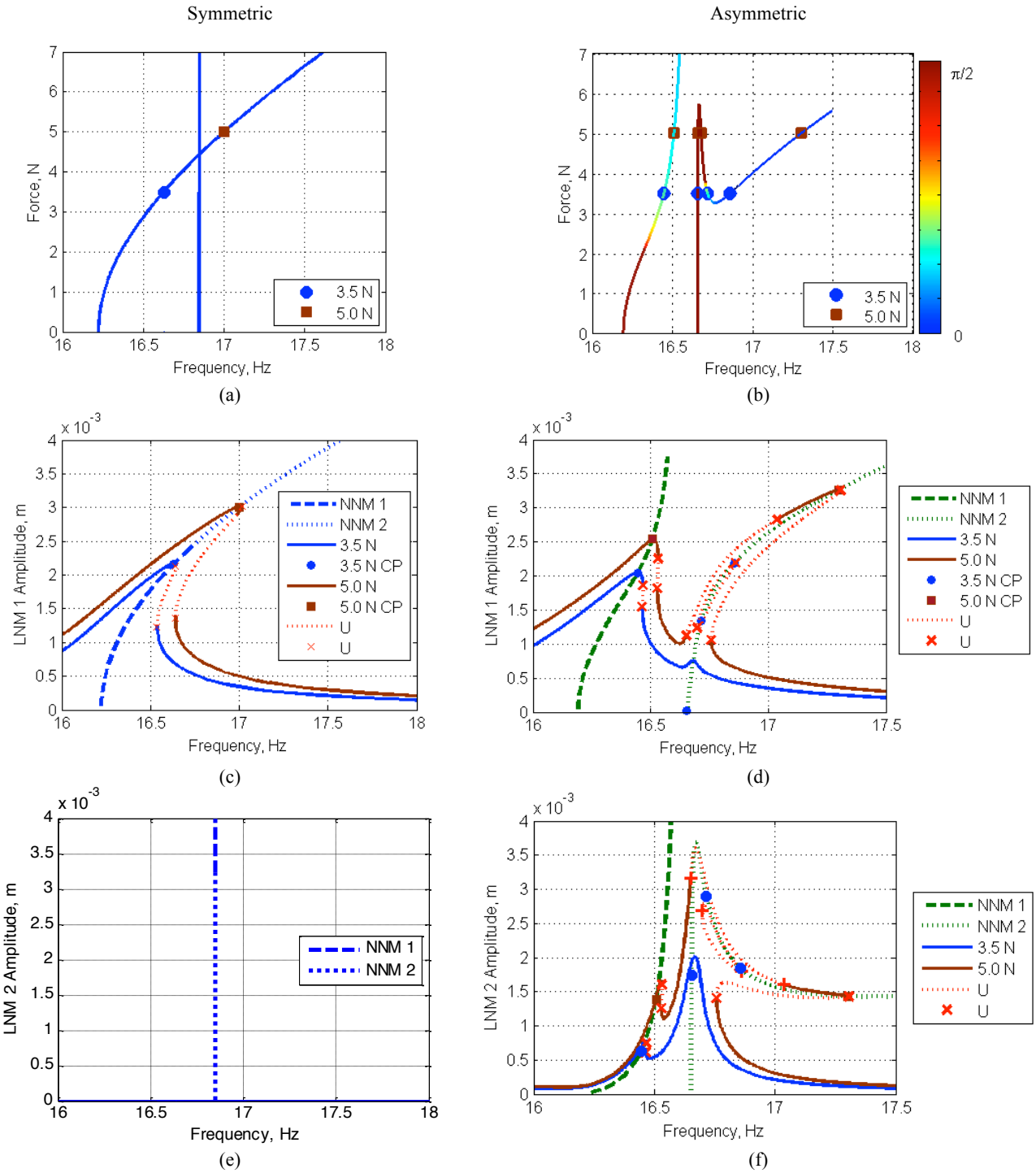

Figure 6: Resonant crossing points and forced response comparison with NNM for the symmetric and asymmetric case where ΔL = -5mm. Validity of the resonant crossing points for the a) symmetric and b) asymmetric systems. Mode 1 response amplitude of the NNM and forced response for the c) symmetric and d) asymmetric systems. Mode 2 response amplitude of the NNM and forced response for the e) symmetric and f) asymmetric systems.

5 Comparison with Experiment

The numerical forced response of the asymmetric system reveals complex nonlinear modal interactions that are of particular interest for this investigation. In this section, we seek to validate this model with an experiment and demonstrate how these modal interactions, which have been shown to be governed by the symmetry of the system manifest in a physical structure. Since the modal interaction is only observed in the asymmetric system, the presented results are demonstrated using a similar asymmetric configuration. It should be noted here that the experimental realisation of the modal interaction is difficult to obtain due to its unstable nature. Therefore, an exact quantitative comparison between model and experiment is not presented at this time. Instead the experimental response of the

structure is qualitatively explored in the region of the quasi-periodic modal interaction using an open loop shaker voltage sine sweep.

5.1 Physical Response and Forcing Comparison

From the resonant crossing point analysis, the shaker voltage is chosen to provide a forcing amplitude near 5N so as to push the structure into the nonlinear veering region. The response at a single point on the cross-beam which is 10cm from the centre of the beam is shown in Fig. 7 for the numerical and experimental tests. Since the modal interaction of interest is concentrated around the second NNM, the frequency sweep of both experiment and numerical systems was started slightly before the second linear mode of vibration to provide similar sweep results. No model updating was applied, and so the model exhibits a 10.7% difference between the second linear natural frequency of the numeric model and physical system. To account for this, a different starting and ending frequency was used for the two sweeps. The results of the numerical sweep are presented in Figs. 7a and 7c, and the experimental sweep is presented in Figs. 7b and 7d. Figures 7a and 7b show the displacement response at L_1 on the cross-beam tip of the structure to the forward sweep for the numerical model and experimental system. Both the numerical simulation and experimental test reveal two distinct behaviors: periodic behavior and quasi-periodic behaviour, which is seen as a response similar to beating in the sweeps. More detailed analysis of these dynamic behaviours is presented in Section 5.3.

Along with the difference between numerical and experimental natural frequencies, a number of other assumptions made in the model could lead to a difference between the dynamic responses; for example, modal damping, fixed boundary conditions, perfect initial geometry, unmodeled modes, and flawless periodic forcing. Specific attention is called to the difference in the applied force for each system, which is shown in Figs. 7c and 7d. For the numerical system, a constant amplitude sine sweep of 5N is applied to the structure, whereas the applied force in the physical system requires the attachment of a shaker. The measurement shown in Fig. 7d is the force directly 'seen' by the structure. Throughout the sweep the shaker resists the 'beating' observed in the unstable region of the response as well as the sharp transition after the second stable region, which appears as a sharp transition in the amplitude of the force. The difference in applied force points to an important difference between these two tests, which could be overcome by implementing advanced strategies to control the input force [31]. The strong interaction observed between the shaker and structure for the experimental system calls into question the validity of the experimentally-measured response; however, a further examination of the dynamic response reveals similar characteristics between the numerical and experimental systems.

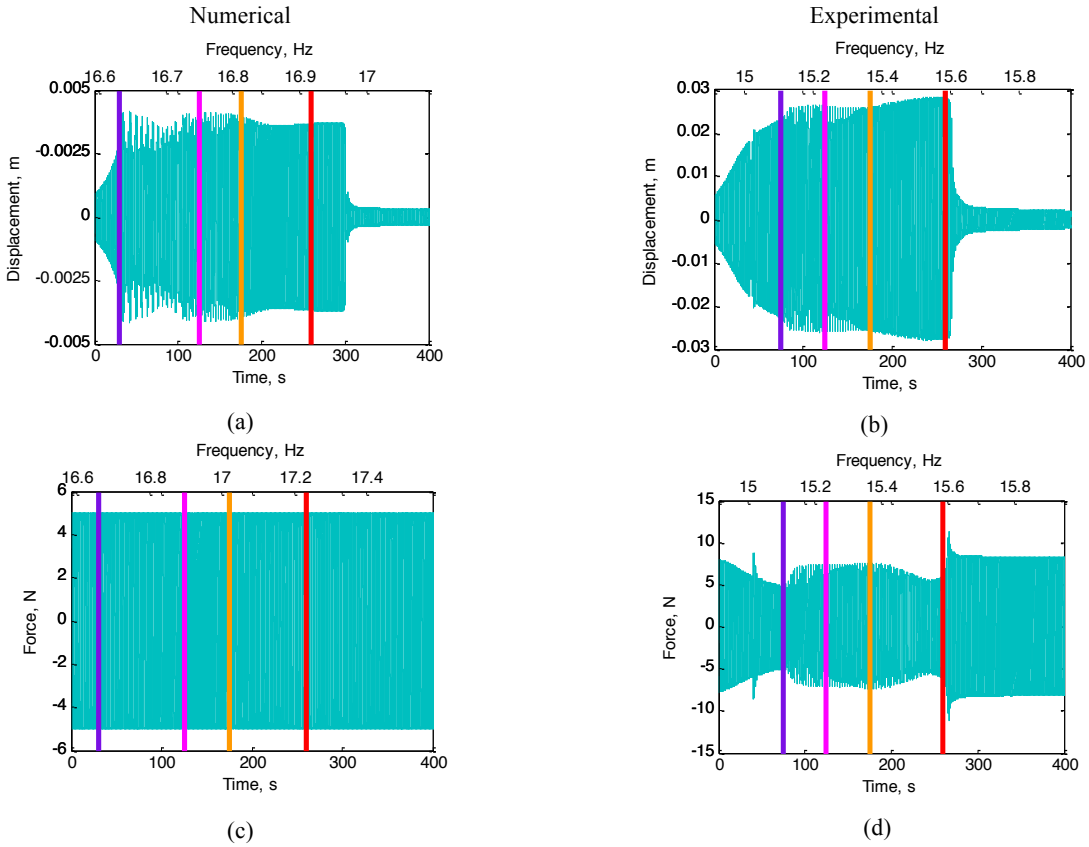

Figure 7: Summary of the sweep results for the numerical (a & c) and experimental (b & d) systems when forced near the second linear normal mode of each system. The dynamic response of the numerical (a) and experimental (b) systems is presented when subjected to forward sine sweeps.

5.2 Modal Domain Response Comparison

Since the system is expected to oscillate in the first two linear modes of vibration of the structure, it is beneficial to project the physical response into the linear modal domain. This projection (shown in Fig. 8) emphasises that the

frequency region of the sweep involves a transition from a mode 2 dominate response to a mode 1 dominated response, as seen in Figs. 8a and 8b for the numerical and experimental system, respectively. Again, qualitative differences are observed between the numerical and experimental systems, but the three regions previously discussed are clear. The first region, between the y-axis and the purple line or 0s to 30s for the model and 0s to 75s for experiment, demonstrates a mode 2 dominated response with the amplitude of mode 1 increasing. The second region, between the purple and red lines or the end of first region up to 225s for the model and 260s for the experiment, demonstrates a significant quasi-periodic energy exchange between mode 1 and mode 2. An equal amplitude in both modes occurs in the second region near 75s for the numerical system and 125s for the experimental system. However, this region also demonstrates the greatest qualitative difference between the numerical and experimental system in the dynamic response, which is potentially due to the shaker-structure interaction. The third region, from the red line to then end of the sweep or 220s to 295s for the numerical system, and 250s to 260s for the experimental system, demonstrates a high-energy mode 1 dominated response before the sharp transition to a low energy mode 1 dominated response indicating a fold bifurcation as designated in Fig. 6.

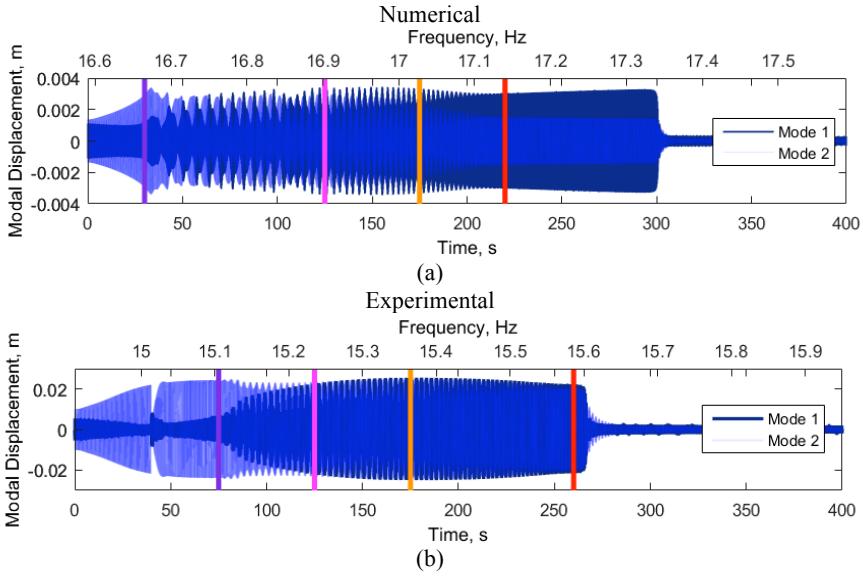

Figure 8: Examination of modal domain response for the numerical (a) and experimental (b) system when subjected to a forward sweep around the second linear normal mode.

A detailed inspection of the second region, specifically at the magenta line or near 125s, reveals similar characteristics of the energy exchange between mode 1 and mode 2 for the numerical and experimental systems. One period of this quasi-periodic exchange of energy is shown in Fig. 9a and 9b. It is observed that, as mode 1 reaches a maximum peak displacement, the phase between mode 1 and mode 2 is zero for both systems. On either side of this inflection point, the peak amplitude of mode 2 lags (or leads) the peak amplitude of mode 1 until mode 1 reaches a minimum peak displacement and another inflection point. The amplitude and phase modulation observed in both systems reveal similar mechanisms influencing the dynamics in this region.

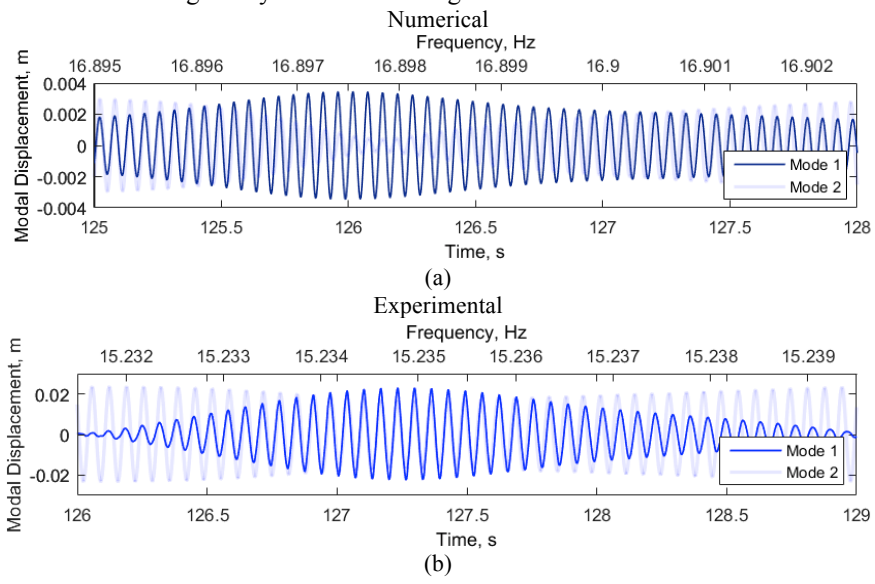

Figure 9: Examination of modal domain response near 125s for the numerical (a) and experimental (b) system

5.3 Phase Portrait Comparison

To investigate the dynamic behaviour within the quasi-periodic response region, a comparison between the structure of the dynamic responses of the numerical and experimental systems is presented in Fig. 10. The structure of the dynamic response is presented as a 3D projection of the phase portrait in terms of the mode 1 displacement (q_1), mode 2 displacement (q_2), and mode 1 velocity ($\dot{q}_1$). Four phase portraits are compared at each of the vertical coloured lines shown in Figs. 7 and 8. Figures 10a & 10b correspond to the purple line and show periodic behaviour (although some deviation from the orbit is seen due to the transient nature of a sweep). As the response enters the quasi-periodic region, near the magenta line (Figs. 10c & 10d), the interaction between mode 1 and mode 2 form a manifold, resembling a torus, which evolves throughout the sweep. This evolution is demonstrated in Figs. 10e & 10f, where a manifold corresponding to the dynamics at the orange line is shown. This clearly demonstrates the nature of the quasi-periodic behaviour. Finally, the red line marks the return of periodic behaviour, shown in Figs. 10g & 10h. In all cases, the qualitative characteristics of the manifold match between the numerical and experimental system well providing further confirmation that the dynamic behaviour of this system is captured by the numerical model.

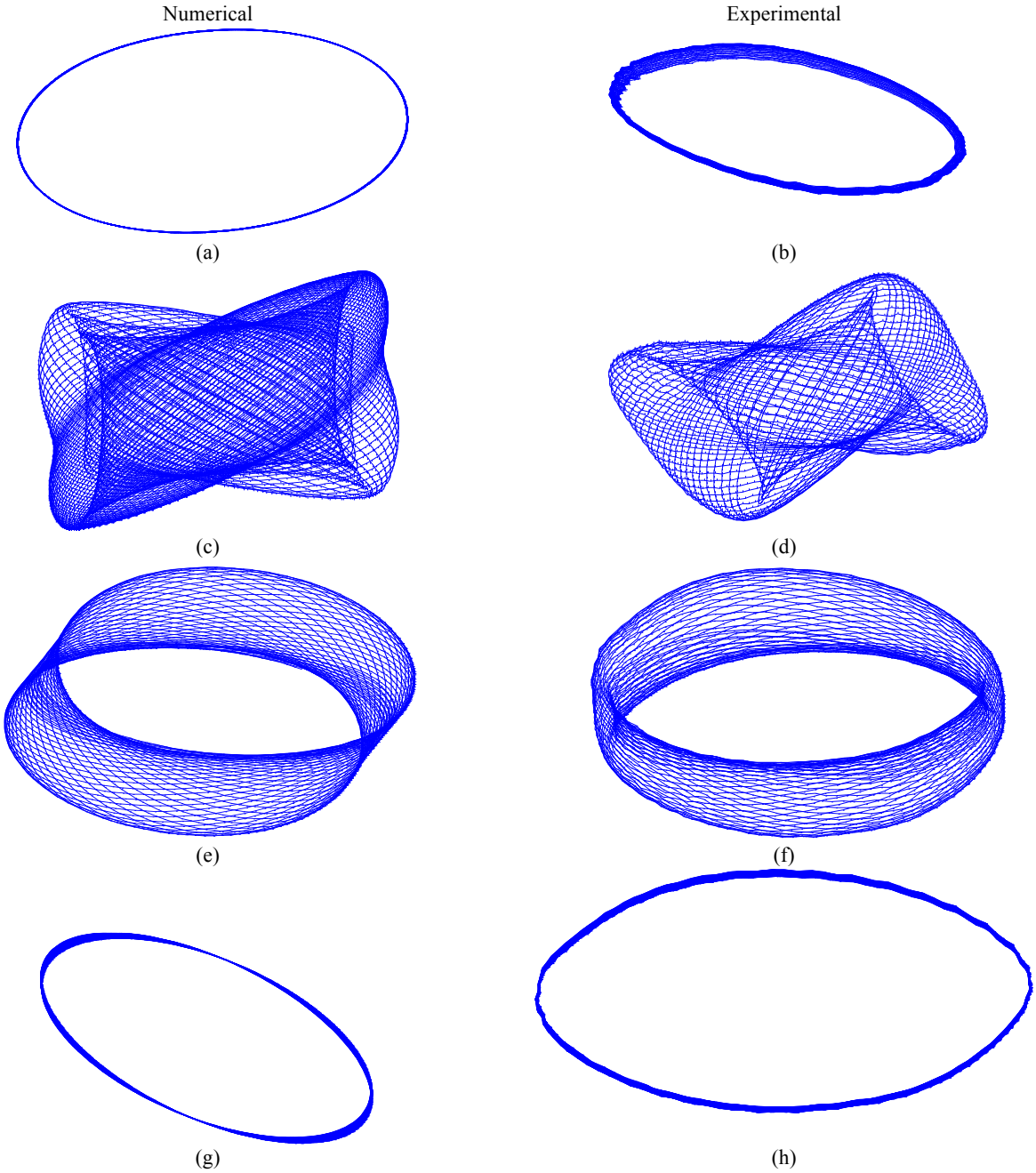

Figure 10: 3D projection of response manifolds using the displacement of mode 1 (q_1) vs. displacement of mode 2 (q_2) vs. velocity of mode 1 ($\dot{q}_1$) at the purple line (a &b), magenta line (c & d), orange line (e & f), and red line (g & h) of the sweep for the numerical (a, c, e, & g) and experimental (b, d, f, and h) systems.

6 Conclusions

In this work, the phenomena of linear modal crossing and veering have been compared to analogous behaviours in nonlinear responses. This has been demonstrated using a clamped-clamped beam, which has a second perpendicular beam attached to it at the mid-span. This second beam supports two movable tip masses, allowing the structure to be tuned. Specifically, the masses allowed the proximity of the first two linear natural frequencies, and the degree of asymmetry of the structure to be adjusted. This allowed the linear crossing and veering phenomena to be demonstrated for a variety of symmetric and asymmetric configurations.

To capture the dynamic tension seen at large deflections, a nonlinear reduced-order model was developed and its predictions of the dynamic behaviour were validated. This model describes the underlying conservative system, the periodic responses of which are termed NNMs. To gain understanding of the modal interactions that may occur in this system, the NNMs were computed using an analytical method. These solutions revealed that the system could exhibit crossing- and veering-like behaviour as a result of the nonlinearity at large deflections. As with the linear case, the nonlinear analogue of the crossing phenomenon is exhibited when the structure is symmetric; likewise, a veering-like behaviour is seen when the structure is asymmetric. In contrast, however, these nonlinear phenomena do not require any structural change to the system, but the crossing and veering are instead dictated by the amplitude of response. It was also shown that the nonlinear veering is a result of the 1:1 interaction between the first two modes – analogous to the cross-correlation of the mode shapes (or eigenvectors) in the linear veering case.

The forced behaviour of the system was firstly considered by examining the relationship between the forced responses, and the NNM branches, or backbone curves. This was achieved using energy transfer analysis, which predicts the points at which the forced responses cross the backbone curves at resonance. These resonant crossing points were then computed for a variety of different forcing amplitudes, revealing how the modal interactions manifest in the forced responses. Finally, the forced responses of the numerical model were compared to the forced data found from experimental tests. This revealed a good qualitative agreement and it was demonstrated that the quasi-periodic behaviour was captured by the model.

Acknowledgements

The authors would like to acknowledge their funding sources, David Ehrhardt is supported by the Engineering and Physical Sciences Research Council EP/K003836/2, Thomas Hill and Simon Neild are supported by EP/K005375/1, and Jonathan Cooper is supported by Royal Academy of Engineering. All data supporting this work are provided as supplementary information accompanying this paper.

References

[1] R.H. Scanlan, and Rosenbaum, R.A., Introduction to the Study of Aircraft Vibration and Flutter, Macmillan, New York, 1951.
[2] K. Worden, and Tomlinson, G.R., Nonlinearity in Structural Dynamics: Detection, Identification, and Modeling, Institute of Physics Publishing, Bristol and Philadelphia, 2001.
[3] R. Brincker, and Lopez-Aenlle, M., Mode Shape Sensitivity of Two Closely Spaced Eigenvalues, Journal of Sound and Vibration, 334 (2015) 377-387.
[4] A.W. Leissa, On a Curve Veering Aberration, Journal of Applied Mathematics and Physics, 25 (1974) 99-111.
[5] N.C. Perkins, and Mote, C.D., Comments on Curve Veering in Eigenvalue Problems, Journal of Sound and Vibration, 106 (1986) 451-463.
[6] R.J. Allemang, The Modal Assurance Criterion (MAC): Twenty Years of Use and Abuse, in: XX International Modal Analysis Conference, Los Angeles, CA, 2002.
[7] R.W. Doll, and Mode, C.D., On the Dynamic Analysis of Curved and Twisted Cylinders Transporting Fluids, Journal of Pressure Vessel Technology, 98 (1976) 143-150.
[8] M.S. Triantafyllou, The Dynamics of Taut Inclined Cables, The Quarterly Journal of Mechanics and Applied Math, 37 (1984) 421-440.
[9] M. Behbahani-Nejad, and Perkin, N.C., Freely Propagating Waves in Elastic Cables, Journal of Sound and Vibration, 196 (1996) 189-202.
[10] J.L. Du Bois, Adhikari, S., and Lieven, N.A.J., Experimental and Numerical Investigation of Mode Veering in a Stressed Structure, in: IMAC XXV, Orlando, Florida, 2007.
[11] W. Lacarbonara, Arafat, H.N., and Nayfeh, A.H., Nonlinear Interactions in Imperfect Beams at Veering, International Journal for Nonlinear Mechanics, 20 (2005) 987-1003.
[12] H.C. Chan, and Liu, J.K., Mode localization and frequency loci veering in disordered engineering structures, Chaos, Solitons & Fractals, 11 (2000) 1493-1504.
[13] B. Balachandran, and Nayfeh, A.H., Observation of Modal Interactions in Resonantly Forced Beam-Mass Structures, Nonlinear Dynamics, 2 (1991) 77-177.
[14] A.I. Manevitch, and Manevitch, L.I., Free Oscillations in Conservative and Dissipative Symmetric Cubic Two-degree-of-freedom Systems with Closed Natural Frequencies, Meccanica, 38 (2003) 335-348.

[15] A.H. Nayfeh, Nonlinear Interactions: Analytical, Computational, and Experimental Methods, New Your, NY, 2000.
[16] W. Lacarbonara, and Rega, G., Resonant Nonlinear Normal Modes Part II: Acitivation/Orthogonality Conditions for Shallow Structural Systems, International Journal for Nonlinear Mechanics, 38 (2003) 873-887.
[17] G. Kerschen, M. Peeters, J.C. Golinval, A.F. Vakakis, Nonlinear normal modes, Part I: A useful framework for the structural dynamicist, Mechanical Systems and Signal Processing, 23 (2009) 170-194.
[18] S.A. Neild, Champneys, A.R., Wagg, D.J., Hill, T.L., and Cammarano, A., The use of normal forms for analysing nonlinear mechanical vibrations, Philosophical Transactions of the Royal Society A, 373 (2014).
[19] R.J. Kuether, Renson, L., Detroux, T., Grappasonni, C., Kerschen, G, and Allen, M.S., Nonlinear Normal Modes, Modal Interactions, and Isolated Resonance Curves, Journal of Sound and Vibration, 351 (2015) 299-310.
[20] T.L. Hill, Cammarano, A., Neild, S.A., and Wagg, D.J., Interpreting the Forced Response of a Two-Degree-of-Freedom Nonlinear Oscillator using Backbone Curves, Journal of Sound and Vibration, 349 (2015) 276-288.
[21] R.W. Gordon, and Hollkamp, J.J., Reduced Order Models for Acoustic Response Prediction, in, Air Force Research Laboratory, 2011.
[22] ABAQUS Documentation, in: D. Systèmes (Ed.), Providence, RI, USA, 2017.
[23] D. Wagg, and Neild, S.A., Nonlinear Vibration with Control, Springer International Publishing, Switzerland, 2015.
[24] R.J. Kuether, and Allen, M.S., A numerical approach to directly compute nonlinear normal modes of geometrically nonlinear finite element models, Mechanical Systems and Signal Processing, 46 (2014) 1-15.
[25] R.J. Kuether, Deaner, B., Allen, M.S., and Hollkamp, J.J., Evaluation of Geometrically Nonlinear Reduced Order Models with Nonlinear Normal Modes, AIAA Journal, 53 (2015) 3273-3285.
[26] N.E. Dowling, Mechanical Behavior of Materials, Third ed., Pearson Prentice Hall, Upper Saddle River, New Jersey, 2007.
[27] T.L. Hill, Neild, S.A., and Cammarano, A.,, An analytical approach for detecting isolated periodic solution branches in weakly-nonlinear structures, Journal of Sound and Vibration, 379 (2016) 150-165.
[28] M.S. Allen, Global and Multi-Input-Multi-Output (MIMO) Extensions of the Algorithm of Mode Isolation (AMI), in: George W. Woodruff School of Mechanical Engineering, Georgia Institute of Technology, Atlanta, Georgia, 2005.
[29] A.D. Shaw, Hill, T.L., Neild, S.A., and Friswell, M.I., Periodic responses of a structure with 3:1 internal resonance, Mechanical Systems and Signal Processing, 81 (2016) 19-34.
[30] M. Peeters, Viguie, R., Serandour, G., Kerschen, G., and Golinval, J.C., Nonlinear Normal Modes, Part II: Toward a Practical Computation using Numerical Continuation Techniques, Mechanical Systems and Signal Processing, 23 (2009) 195-216.
[31] L. Renson, Gonzalez-Buelga, Barton, D.A.W., and Neild, S.A., Robust identification of backbone curves using control-based continuation, Journal of Sound and Vibration, 367 (2016) 145-158.